IEEE Access
Multidisciplinary | Rapid Review | Open Access Journal

Received December 21, 2021, accepted January 11, 2022, date of publication April 14, 2022, date of current version April 25, 2022.

Digital Object Identifier 10.1109/ACCESS.2022.3167432

Metamaterial Liner for MRI Excitation–Part 1: Theory, Modeling and Design

ADAM MITCHELL MAUNDER[1,2], (Member, IEEE), CHRISTOPHER BARKER[2], (Student Member, IEEE), NICOLA DE ZANCHE[1,3], (Senior Member, IEEE), AND ASHWIN K. IYER[2], (Senior Member, IEEE)

[1]Department of Oncology, University of Alberta, Edmonton, AB T6G 1Z2, Canada
[2]Department of Electrical and Computer Engineering, University of Alberta, Edmonton, AB T6G 2V4, Canada
[3]Alberta Health Services, Edmonton, AB T5J 3E4, Canada

Corresponding author: Adam Mitchell Maunder (amaunder@ualberta.ca)

This work was supported in part by the Alberta Innovates Postdoctoral Fellowship in Health Innovation and Research Grants from the Natural Sciences and Engineering Research Council (NSERC) of Canada Discovery Grants Program.

ABSTRACT This work details the practical and theoretical concepts underlying the design of a metamaterial (MM) liner for magnetic resonance imaging (MRI) radio frequency (RF) excitation. The Part 2 companion to this paper details the practical design and performance comparison to a conventional birdcage coil. The operation of the MM liner relies on specifically engineered effective permittivity and permeability of a thin liner on the inner surface of the MRI bore, to enable the propagation of electromagnetic (EM) waves at frequencies below the natural-cutoff of the bore itself. Here, the effective anisotropic EM properties of the MM liner structure are calculated by a combined circuit- and effective-medium model, and the analytical dispersion characteristics are compared to full-wave eigenmode simulations. The results of the effective medium model representation of the MM liner agree fundamentally with simulation. The model may thus assist the design and tuning of the liner to achieve a standing-wave resonance with field distribution and mode spacing suitable for MRI RF excitation. The transmission properties and EM fields of a full-scale MM lined bore for $B_0 = 4.7$ T MRI are simulated including realistic losses. These methods enable robust design of thin MM liners for arbitrary bore sizes and B_0 field strengths.

INDEX TERMS Coil, effective medium, magnetic resonance imaging, MRI, metamaterial, radiofrequency, ultra-high field, waveguide.

I. INTRODUCTION

Increasing magnetic field strength (B_0) has been a consistent trend in magnetic resonance imaging (MRI) due to the associated increase in image signal-to-noise (SNR) [1]. However, even at 3 Tesla (T), with a Larmor frequency of 128 MHz for standard ^{1}H (proton) imaging, the wavelength in the high-permittivity bulk of the human body is ∼30 cm, which results in regions of signal inhomogeneity and increased local specific absorption rate (SAR) from the constructive and destructive interference of the RF fields produced during MR excitation pulses. These fields must be tuned to the Larmor frequency and provide a homogeneous, transverse, and circularly polarized magnetic field with limited local SAR.

The associate editor coordinating the review of this manuscript and approving it for publication was Shah Nawaz Burokur.

RF inhomogeneity [2] and local SAR constraints [3] are limiting factors to the adoption of >3 T field strengths for clinical use [4]. Thus, at field strengths >3 T MRI has been largely limited to single-organ investigation using targeted or "shimmed" RF fields (analogous to beamforming) [5], or head imaging [6], rather than whole-body imaging.

Whole-body volume resonators, specifically the birdcage coil, become difficult to construct and employ at field strengths >3T, but designs of the transverse electromagnetic (TEM) coil for 4.7T [7] and 7T body imaging have been demonstrated. However, the homogeneity and efficiency at these fields strengths with all volume resonators have been unsatisfactory. Therefore, ≥ 4 T field strength MRI systems generally do not include a body-coil and it has become state-of-the-art to employ transmit arrays (>8 elements) with power/phase RF shimming techniques [4] to target specific organs and eliminate field nulls. The enduring issues

This work is licensed under a Creative Commons Attribution 4.0 License. For more information, see https://creativecommons.org/licenses/by/4.0/

of homogeneity and transmit efficiency, the complexity of employing transmit arrays and the feasibility of real-time SAR prediction and monitoring are current limiting factors in adopting >3T MRI clinically for thoracic or abdominal imaging. Thus, there is still no standard transmit excitation method for providing uniform MR excitation over the field-of-view of the body and other approaches are needed.

One way to improve the homogeneity of MR signal excitation and reduce the local SAR is to employ traveling waves excited by antennas placed at the ends of the MRI bore [8]. However, there are several key drawbacks with the traveling-wave MRI approach:

1. Propagation of the MR-relevant fundamental waveguide mode (TE_{11}) only occurs above the natural cutoff frequency of the cylindrical scanner bore, which is only achievable with high field strengths (e.g., 7 T – 298 MHz) and wide bores (60–70 cm diameter). Conversely, propagating modes are completely cut off in human-sized scanners operating below approximately 7 T.
2. Low transmit efficiency that must be compensated for by higher transmit power.
3. Wave reflections at air-body interfaces result in destructive interference and unpredictable regions of low signal in the body, in addition to the constructive-destructive interference of standing waves in the body typical with conventional resonators [9].
4. Longitudinal field attenuation due to losses in the body.

A further challenge for adoption of traveling wave MRI is the dependence of the phase velocity on the MR frequency and geometry of the waveguide. Without control of the phase velocity, multiple wavelengths (analogous to longitudinal modes) may occur along the length of the bore ($\sim$2m) depending on the longitudinal propagation constant, resulting in nulls and hot spots, which reduce efficiency and homogeneity. Due to these drawbacks, improved SAR and homogeneity have not been achieved with basic traveling-wave MRI compared to localized methods of excitation (birdcage or TEM coils) [10].

Approaches have been proposed to address these issues. The bore can be partially filled with adjustable dielectric rods to reduce the cutoff and permit the propagation of higher-order modes [11], thus also providing additional degrees of freedom for field control. However, this is a complex and cumbersome method which also decreases the available bore space. Indeed, larger bore space is often needed to accommodate larger subjects, alleviate claustrophobia, and increase comfort. The use of a coaxial conductive waveguide with a central gap at the imaging region permits controllable and predictable field production and helps to focus the fields onto the imaging region, but also occupies significant space in the bore and confines the patient inside a narrow, albeit flexible, tube [12]. Similarly, lining the surface of the bore with high-dielectric-permittivity rods enhances the focusing of the field in the desired central region of the bore, reduces the attenuation in the longitudinal direction and lowers the frequency for propagation, but requires a thick liner (10 cm) and does not improve the low efficiency [13].

Additional modifications of the traveling-wave paradigm include ring structures that focus the field and are also attractive because the bore center is accessible. For example, the annular ladder resonator [14], pairs of rings made of transverse dipoles laid end-to-end [15] or the use of ''conformal resonant right-/left-handed'' antennas [16], [17], have all been shown to improve the centrally localized transmit efficiency of traveling wave MRI. However, the inner diameters of the rings in these three examples reduced the accessible bore diameter by 8 cm, 10 cm and 13 cm, respectively, thus occupying an impractical amount of space. Furthermore, these structures are designed for 7 T (298 MHz), and propagation of the TE_{11} mode is already achieved with these bore diameters, so the rings are not designed to allow operation at the lower frequencies of clinical scanners, or at 4.7 T as in this study. Finally, these previous ring structures lack a complete theoretical description to guide their design, and their use has been demonstrated only with a few elements producing a limited field of view and homogeneity.

This work explores the use of metamaterials (MMs), which are engineered structures consisting of an array of scatterers designed to produce a desired exotic macroscopic EM response for sufficiently long wavelengths [18], [19]. MMs have been used in MRI to focus and control the transmit and receive RF fields. For example, to improve the localized receive sensitivity of individual elements [20]–[24]. Transmit structures have also been developed [25], [26], but comparison to established RF resonators or ''coils'' is still lacking.

The theoretical description of below-cutoff propagation in circular waveguides by a MM liner with epsilon-negative and near zero (ENNZ) was first described by Pollock and Iyer [27]. Propagation can be far below the natural waveguide cutoff with a backwards-dispersion relation for the hybrid electric (HE) and hybrid magnetic (EH) modes [28] (analogous to the transverse electric (TE) and transverse magnetic (TM) modes of a homogeneously filled circular waveguide). The HE_{11} mode provides a uniform H-field conducive to MR excitation. The practical realization of an ENNZ liner was achieved by azimuthally segmented periodic ring structures with radially-directed inductors and capacitive gaps between thin-wire sections [29]–[31]. Below-cutoff propagation was demonstrated for waveguides $\sim$3 cm in diameter operating at $\sim$3.7 GHz (approximately 43% below their natural cutoff), suggesting that such MM liners could be scaled to permit traveling-wave MRI for fields <7 T and small-bore diameters where cutoff of the TE_{11} mode is not achieved naturally [32], [33].

However, previous works did not provide a comprehensive theory of the magnetic response (characterized by the effective permeability) of the MM structure or provide a rigorous model of how the permittivity and permeability vary with the circuit parameters, topology or geometry of the structure.

Thus, this work describes a more complete effective-medium model (EMM) of the circuit layout of the MM liner rings to guide the design and optimization of the MM liner for the MRI bore. The method of analysis developed for determining the effective-medium values of a periodic ring structure has not been described previously to the best of our knowledge. Unlike the previous Drude model applied for permittivity to describe all modes, the parameters derived here are spatially dispersive: the effective permeability and permittivity depend on wave-vector. Consequently, they are fundamentally non-local.

There are four criteria for locality: passivity, causality, absence of radiation losses and independence of the material parameters on the propagation direction [34], [35]. Ideally, to have physical, rather than phenomenological meaning, the constitutive parameters derived from a material homogenization method should follow the criteria for locality, but even the most used homogenization methods only do so in the long-wavelength limit of propagation; these include Bloch transmission analysis [36], [36] scattering parameter reflection and transmission retrieval [37] and field averaging [38], [39]. Furthermore, parameter extraction in the case of anisotropic materials is ambiguous beyond very simple cases (such as from a slab of material), and results of homogenization can be highly inaccurate in the case of resonant and/or asymmetric structures, where homogenization procedures are expected to fail, or be inapplicable [37].

Thus, although it is desirable to characterize a MM as a homogenous medium with a local constitutive relation analogous to natural materials, such a description would not accurately represent the non-local exotic electromagnetic interaction/response of many MM to different excitations and across all frequencies. For this reason, the use of non-local constitutive parameters has been proposed and various methods have been established [40]–[42]. The loss of a direct physical relation is compensated for by better predictive accuracy of the electromagnetic response of MM structures. The case of multilayered dielectric media is the most well-established case where the use of non-local homogenization schemes more accurately describes the reflection/transmission from different incident angles [43], [44].

The MM liner presented in this study is a particular case where non-local constitutive parameters may be required to better characterize the electromagnetic response of the ring structure. Its circularly periodic and segmented structure results in resonant and highly non-local response, which is highly dependent on the azimuthal mode order. Thus, the EMM developed is a non-local homogenization procedure.

An advantage of the MM liner concept and design is that it is scalable for different frequencies and MRI bore or waveguide sizes. To achieve the desired mode propagation for any specific bore size, frequency, or MM liner thickness, only the target effective medium parameters will change. Thus, the choice of the field strength (1.5T, 3T, 4.7T, 7T, etc.) is immaterial to the validation of the methods developed here and the results can be extrapolated to any field strength.

Preliminary comparison studies of clinical applications of abdominal or thoracic imaging for MRI field strengths of 4T-4.7T vs. 1.5T demonstrated the expected boost in signal-to-noise, resulting in improved image quality [45], [46]. However, at high field strengths the SAR constraints and inhomogeneity limit many clinically relevant imaging sequences (spin-echo, steady state free precession, diffusion weighted imaging, etc.) [47]. For applications dependent on those sequences, comparison studies of 4T vs. 1.5T [48], as well as at 7T compared to 1.5T or 3T [49], have therefore demonstrated poorer performance. If the limitations of SAR and inhomogeneity were reduced for 4T-4.7T imaging the benefit of improved imaging quality could be obtained for a wider range of imaging sequences, stimulating clinical adoption and increased research interest of field strengths higher than 3T for thoracic and abdominal imaging. This potential has encouraged research to address the challenges of ultra-high-field abdominal and thoracic imaging, most of which has been performed at 7T due to the greater number of whole-body systems in operation compared to 4.7T. We believe that since 4.7T is the first available field strength higher than 3 T to provide an SNR gain without a drastic reduction in wavelength (e.g., 7 T), it is an optimal target to develop and test new methods of excitation that attempt to improve the SAR or transmit homogeneity and enable new imaging studies that have not been feasible at 4.7T to date. Any resulting improvements with the MM liner may then be extended to any other field strength with similar designs scaled to the appropriate frequency.

The objectives of this study, along with the companion paper [50], are to 1) outline a comprehensive method that can be used to design the MM liner with EMM for any field strength (1.5T, 3T, 4.7T, 7T etc.); 2) demonstrate whether the MM liner can provide a homogeneous transmit field suitable for MRI; and 3) enable thoracic and abdominal imaging studies 4.7T with a practical whole-body transmit resonator design.

The present work outlines the theory and design of MM liners for MRI as follows: Section II derives an EMM of the MM liner. Section III compares the dispersion relation calculated using the EMM to that of the full-wave simulation. Finally, section IV presents the simulation of an MM-lined waveguide designed for MR excitation at 200 MHz (4.7 T) using the HE_{11} mode operating as a $\lambda/2$ resonator. The outcome of this study is a robust methodological framework for designing MM liners for MRI at any field strength.

II. THEORY

The MM-lined MRI bore is approximated by the structure shown in Fig. 1(a/b), comprising a cylindrical waveguide of radius b, an accessible region with free-space permittivity (ε_0) and permeability (μ_0), and a thin interior liner of thickness $t_r = b - a$ with cylindrically anisotropic material properties that take the form of diagonal tensors: $\overline{\overline{\varepsilon}}_l = \varepsilon_0 \mathrm{diag}(\varepsilon_r, \varepsilon_\phi, \varepsilon_z)$

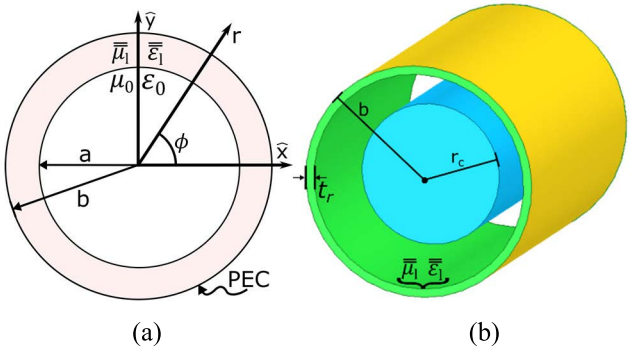

FIGURE 1. (a) Cross-section of a MM lined cylindrical waveguide with labelled electromagnetic parameters and (b) conceptual diagram of MRI bore with cylindrical phantom load and anisotropic MM liner.

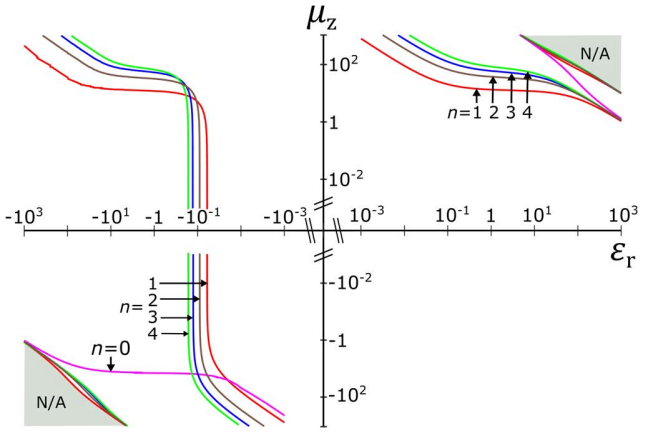

FIGURE 2. loci of μ_z and ε_r corresponding to cutoff $f_0 = 200$ MHz for HE_{n1} modes (n = 0 (magenta), n = 1 (red), n = 2 (brown), n = 3 (blue), n = 4 (green)) for, $a = 0.269$ m and $b = 0.280$ m. Regions where solutions are too crowded together to show clearly are shaded in gray and labelled N/A.

and $\overline{\overline{\mu}}_l = \mu_0 \text{diag}(\mu_r, \mu_\phi, \mu_z)$. To generate the desired HE_{11} mode for MR excitation it is necessary to determine the cutoffs and dispersion characteristics of this structure.

A. MODE CUTOFF FREQUENCIES AND FIELDS

In the case of biaxial permittivity and permeability, where $\overline{\overline{\varepsilon}}_l = \varepsilon_0 \text{diag}(\varepsilon_r, \varepsilon_r, \varepsilon_z)$ and $\overline{\overline{\mu}}_l = \mu_0 \text{diag}(\mu_\phi, \mu_\phi, \mu_z)$, the analysis is simplified, and the cutoffs are obtained by [27], [30]

$$\frac{J_n'(k_0 a)}{J_n(k_0 a)} - \frac{\sqrt{\mu_z}}{\sqrt{\varepsilon_r}} \frac{G_n'\left(k_0\sqrt{\varepsilon_r \mu_z} a\right)}{G_n\left(k_0\sqrt{\varepsilon_r \mu_z} a\right)} = 0, \quad \text{for } HE_{n1} \text{ modes} \tag{1a}$$

$$\frac{J_n'(k_0 a)}{J_n(k_0 a)} - \frac{\sqrt{\varepsilon_z}}{\sqrt{\mu_\phi}} \frac{F_n'\left(k_0\sqrt{\varepsilon_z \mu_\phi} a\right)}{F_n\left(k_0\sqrt{\varepsilon_z \mu_\phi} a\right)} = 0, \quad \text{for } EH_{n1} \text{ modes} \tag{1b}$$

$$\text{where } F_n(xa) = Y_n(xb) J_n(xa) - J_n(xb) Y_n(xa), \text{ and} \tag{1c}$$

$$G_n(xa) = Y_n'(xb) J_n(xa) - J_n'(xb) Y_n(xa), \tag{1d}$$

where n is the mode order in the $\hat{\phi}$ direction and J_n and Y_n are the n-th order Bessel and Neumann functions, respectively. The cutoff of the HE_{n1} modes are affected only by μ_z and ε_r, while those of the EH_{n1} modes are affected only by μ_ϕ and ε_z. The complex dispersion behaviour of the EH and HE modes at frequencies away from cutoff depend on all components of the anisotropic permittivity and permeability.

The field analysis of the MM liner presented in Ref. [27] will not be repeated here. However, the calculation of the r-directed E-field and z-directed H-field in the liner region are provided in the supplementary material. The derivation of the approximation that the fields are radially homogeneous within the MM liner region when $nt_r/b \ll 1$ is also provided, which is used in the model in the next section.[1] Fig. 2 shows the μ_z and ε_r required for cutoff of the HE_{n1} modes at the relevant 4.7 T ^{1}H MRI frequency $f_0 = 200$ MHz for $a = 0.269$ m and $b = 0.28$ m.

Previously, radially oriented inductors and azimuthally directed wires separated by capacitive gaps were explored as a method of realizing ε_r that is ENNZ [30], [31] and predict the cutoff of the HE_{11} mode. However, a simple Drude dispersion model of the effective permittivity was applied for all modes, which accurately predicted the cutoff of the EH_{01} mode and only approximated those of the other closely spaced HE_{n1} modes. In the work presented here, only the HE_{n1}(and EH_{01}) are explored, therefore an analytical model that describes μ_z and ε_r with better accuracy is considered in the next section.

B. BILAYER INFINITE CURRENT SHEET

It is necessary for a useful EMM to relate the currents/voltages on the MM structure to the fields within the liner. Thus, to apply the derivation of the MM-lined waveguide propagation characteristics in [27] the electromagnetic representation must describe effective $\overline{\overline{\varepsilon}}_l$ and $\overline{\overline{\mu}}_l$ that are homogeneous, with biaxial permittivity and permeability and confined to the liner region. The electrostatic solution for two layers of longitudinally infinite conducting current sheets in Fig. 3(a) satisfies this requirement, since the scattered radial displacement field ($\vec{\boldsymbol{D}}^{sr}$),

$$\vec{\boldsymbol{D}}^{sr} = \varepsilon_r \varepsilon_0 \vec{E}^{sr} = \varepsilon_r \varepsilon_0 \boldsymbol{V}^{sr}/t_r \hat{r} \tag{2}$$

and the scattered longitudinal magnetizing field ($\vec{H}^{sz}$),

$$\vec{H}^{sz} = \boldsymbol{I}^{\phi}/\Delta z \hat{z}, \tag{3}$$

are confined between the sheets representing the liner region, and zero outside [51]. In this representation, both the scattered radially oriented voltage ($\boldsymbol{V}^{sr}$) and azimuthally directed currents ($\boldsymbol{I}^{\phi}$) are vectors whose indices indicate the position along the azimuthal direction and are calculated for impinging HE_{n1} fields (c.f. next section). Thus, $\vec{\boldsymbol{D}}^{sr}$

[1] Supporting document contains the derived field equations (Supplementary Material I. Radially Homogeneous Field Equations for Metamaterial Liner).

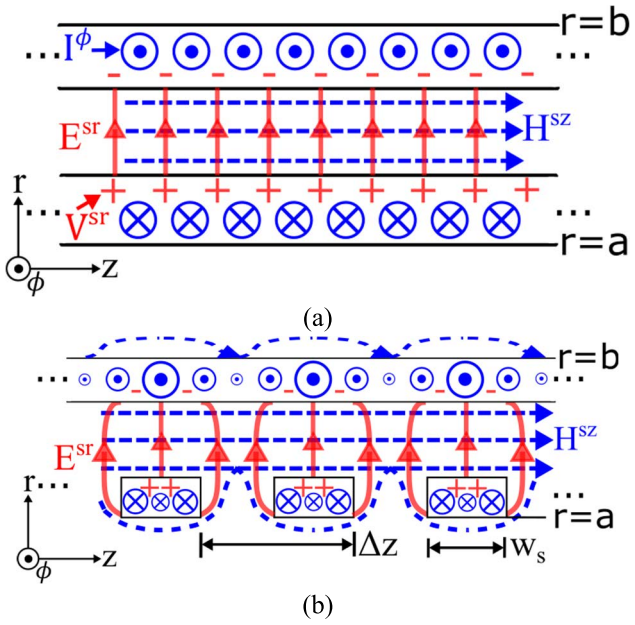

FIGURE 3. (a) Representation of the $\vec{H}^{sz}$ and $\vec{E}^{sr}$ fields due to the induced current I^{ϕ} and voltage V^{sr} in a bilayer infinite current sheet and (b) azimuthally directed rings that approximates the infinite current sheet.

and $\vec{H}^{sz}$ also have an azimuthal variation as defined by the current and voltage distributions. In Fig. 3(b), closely spaced conducting rings with an outer shield are represented as an approximation to the infinite current sheets in (a). This permits the calculation of the effective medium ε_r and μ_z values based on the analysis of the induced currents and voltages on a single ring.

C. EFFECTIVE MEDIUM MODEL OF MM LINER

In this analysis, it is assumed that only $\boldsymbol{I}^{\phi}$ and $\boldsymbol{V}^{sr}$ in the representation of Fig. 3 are present and longitudinally-directed currents or voltages are not induced to alter the effective medium values of μ_{ϕ} or ε_z, thus $\mu_{\phi} = \varepsilon_z = 1$. This assumption allows the analysis of only a single ring in isolation to determine the dispersion of ε_r and μ_z, as shown in Fig. 4(a), in a similar manner to capacitively loaded loops [52] or split-ring resonators [53]. Subsequently, the process described in [27] is used to determine the dispersion characteristics.

The ring structure is generalized to an N_{ϕ}-segment network as depicted in Fig. 4(b), with the N_{ϕ}-th and 1st segments connected. Each segment has a length of $2\pi a/N_{\phi}$, with intrinsic per-unit-length series inductance ($L^{\phi'}_{n_{\phi}}$) and parallel capacitance ($C^{r'}_{n_{\phi}}$). Thus, each segment has an inductance and capacitance of $L^{\phi}_{n_{\phi}} = 2\pi a L^{\phi'}_{n_{\phi}}/N_{\phi}$ and $C^{r}_{n_{\phi}} = 2\pi a C^{r'}_{n_{\phi}}/N_{\phi}$, respectively (assuming short electrical length). For each segment, a lumped radial tuning impedance $Z^{r}_{n_{\phi}}$ is in parallel with $C^{r}_{n_{\phi}}$, and an azimuthal tuning impedance $Z^{\phi}_{n_{\phi}}$ is in series with $C^{r}_{n_{\phi}}$, where n_{ϕ} is the segment number. For segments that do not include lumped impedances $Z^{\phi}_{n_{\phi}} = 0$ and $Z^{r}_{n_{\phi}} = \infty$.

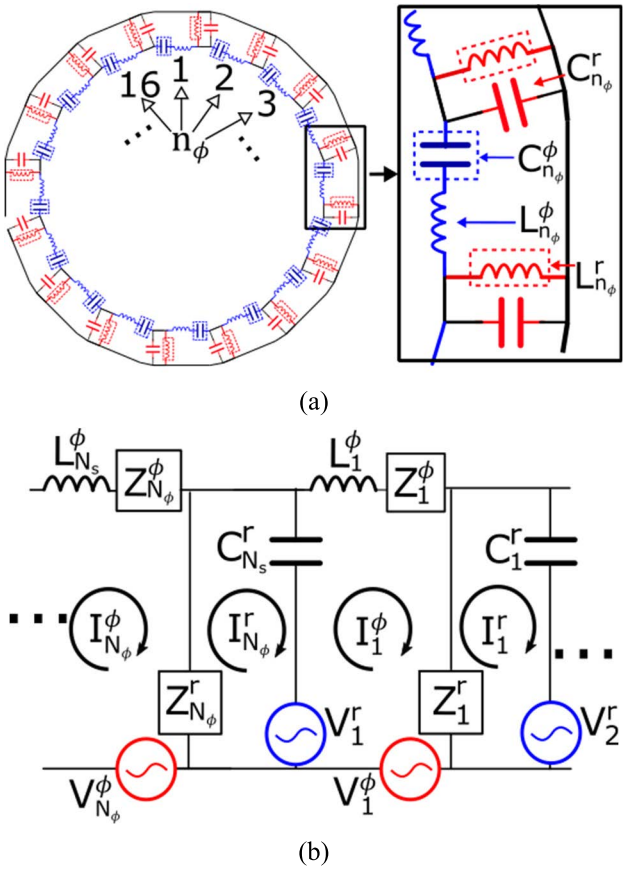

FIGURE 4. (a) Circuit representation of a single ring of the MM liner with lumped loading (surrounded by dashed lines) and intrinsic circuit parameters. (b) The generalized periodic network model of the ladder structure composed of N_{ϕ} $\phi-$ directed and $r-$ directed lumped impedances ($Z^{\phi}_{n_{\phi}}$ and $Z^{r}_{n_{\phi}}$) and intrinsic series inductances ($L^{\phi}_{n_{\phi}}$) and parallel capacitances ($C^{r}_{n_{\phi}}$). Excitations are represented by generators arising from the induced EMFs: V^{ϕ} from $\vec{H}^{iz}$ and V^{r} from $\vec{D}^{ir}$.

The constitutive relations for the effective permeability and permittivity of the liner link the incident fields ($\vec{H}^{iz}$ and $\vec{D}^{ir}$) and scattered fields ($\vec{H}^{sz}$ and $\vec{D}^{sr}$) to the longitudinal magnetic field ($\vec{B}^{z}$) and radial electric field ($\boldsymbol{E}^{r}$) according to

$$\vec{B}^{z} = \mu_z\mu_0\vec{H}^{z} = \mu_0\left(\vec{H}^{iz} + \vec{H}^{sz}\right) \tag{4a}$$

$$\vec{E}^{r} = \vec{D}^{r}/\varepsilon_r\varepsilon_0 = \left(\vec{D}^{ir} + \vec{D}^{sr}\right)/\varepsilon_0. \tag{4b}$$

EMMs have typically been used to describe structures with unit cells (here, a single ring) with dimensions that satisfy the long-wavelength limit (dimensions $\ll \lambda$ [54]). Indeed, this is the case for the radial dimensions, t_r, and longitudinal dimensions, $\gamma\Delta z$, of the ring which are much less than a wavelength. To include the known angular variation the incident fields, $\vec{H}^{iz}$ and $\vec{D}^{ir}$ in the liner are represented by

$$\vec{H}^{iz}(n_{\phi}) = \left|H^{iz}\right| sin\left(2\pi n_{\phi} n/N_{\phi}\right)\hat{z} \tag{5a}$$

$$\vec{D}^{ir}(n_{\phi}) = \left|D^{ir}\right| cos\left(2\pi n_{\phi} n/N_{\phi}\right)\hat{r}. \tag{5b}$$

In these relations the continuous fields are discretized at angular positions $2\pi n_\phi n/N_\phi$ by the N_ϕ segments introduced in the circuit model. The rings are electrically large in the azimuthal direction and so the EMM modelling procedure differs from that of previous methods by considering the sinusoidal azimuthal variation of the field for the different HE_{n1} modes. Typically, uniform plane waves have been assumed [55]. Thus, the effective-medium μ_z and ε_r are found by field averaging [55], [56], also termed the field summation method [57], with the ratio of total fields to the incident fields in the liner region given by

$$\mu_z = \frac{\left(\vec{H}^{\,iz} + \vec{H}^{\,sz}\right) \cdot \vec{H}^{\,iz} / \left|\vec{H}^{\,iz}\right|}{\vec{H}^{\,iz} \cdot \vec{H}^{\,iz} / \left|\vec{H}^{\,iz}\right|} = 1 + \frac{\vec{H}^{\,sz} \cdot \vec{H}^{\,iz} / \left|\vec{H}^{\,iz}\right|}{\left|\vec{H}^{\,iz}\right|_1} \tag{6a}$$

$$\varepsilon_r = \frac{\vec{\boldsymbol{D}}^{\,ir} \cdot \vec{\boldsymbol{D}}^{\,ir} / \left|\vec{\boldsymbol{D}}^{\,ir}\right|}{\left(\vec{\boldsymbol{D}}^{\,ir} + \vec{\boldsymbol{D}}^{\,sr}\right) \cdot \vec{\boldsymbol{D}}^{\,ir} / \left|\vec{\boldsymbol{D}}^{\,ir}\right|} = \frac{1}{1 + \vec{\boldsymbol{D}}^{\,sr} \cdot \vec{\boldsymbol{D}}^{\,ir} / \left(\left|\vec{\boldsymbol{D}}^{\,ir}\right| \left|\vec{\boldsymbol{D}}^{\,ir}\right|_1\right)}. \tag{6b}$$

The dot product of the incident field with itself divided by its magnitude (L^1-norm) represents the field averaged across all segments of the ring. The dot product of the incident field and scattered field represents the correlation of the induced and incident fields. This accounts for the difference in phase or sign/direction of the incident vs. scattered fields along the azimuthal direction.

With the link between the incident and scattered fields and the effective medium properties established by (6a) and (6b), the relation between the currents and voltages induced on the MM ring structure and the scattered fields is presented as follows. The voltages induced on one azimuthal section of the ring by $\vec{\boldsymbol{H}}^{\,iz}(\boldsymbol{V}^\phi)$ and $\vec{\boldsymbol{D}}^{\,ir}(\boldsymbol{V}^{\mathrm{r}})$ are

$$\boldsymbol{V}^\phi_{n_\phi} = -j\omega\mu_0 \vec{H}^{\,iz}_{n_\phi} t_r \pi (b+a)/N_\phi \tag{7a}$$

$$\boldsymbol{V}^{\boldsymbol{r}}_{n_\phi} = \vec{\boldsymbol{D}}^{\,ir}_{n_\phi} t_r / \varepsilon_r \varepsilon_0. \tag{7b}$$

Using network mesh equations, the impedance matrices describing the self-impedance of the $\vec{H}^{\,sz}$-producing meshes ($\boldsymbol{Z}_H$), the self-impedance of the $\vec{\boldsymbol{D}}^{\,sr}$-producing meshes ($\boldsymbol{Z}_E$),and the coupling between meshes ($\boldsymbol{Z}_{HE}$) shown in Fig. 4(b) are, respectively,

$$\boldsymbol{Z}_H(m_\phi, n_\phi) = \begin{cases} Z^\phi_{n_\phi} + Z^r_{n_\phi} + j\omega L^{\boldsymbol{\phi}}_{n_{\boldsymbol{\phi}}} + 1/j\omega C^{\boldsymbol{r}}_{n_{\boldsymbol{\phi}}}, & m_\phi = n_\phi \\ 0, \quad \text{otherwise} \end{cases} \tag{8a}$$

$$\boldsymbol{Z}_E(m_\phi, n_\phi) = \begin{cases} Z^r_{n_\phi} + 1/j\omega C^{\boldsymbol{r}}_{n_{\boldsymbol{\phi}}}, & m_\phi = n_\phi \\ 0, \quad \text{otherwise} \end{cases} \tag{8b}$$

$$\boldsymbol{Z}_{HE}\left(m_\phi, n_\phi\right) = \begin{cases} -Z^r_{n_\phi}, & m_\phi = n_\phi \\ -1/j\omega C^{\boldsymbol{r}}_{n_{\boldsymbol{\phi}}}, & m_\phi = n_\phi + 1 \\ 0, \quad \text{otherwise}. \end{cases} \tag{8c}$$

Because the radially-oriented impedances $Z^r_{n_\phi}$ and $1/j\omega C^r_{n_{\boldsymbol{\phi}}}$ dominate inter-mesh coupling, the intrinsic mutual impedances (i.e., mutual inductances) are neglected. The mesh currents for a given voltage excitation are then found as

$$\begin{bmatrix} \boldsymbol{I}^\phi \\ \boldsymbol{I}^r \end{bmatrix} = \boldsymbol{Z}^{-1}\boldsymbol{V} = \begin{bmatrix} \boldsymbol{Z}_H & \boldsymbol{Z}_{HE} \\ \boldsymbol{Z}'_{HE} & \boldsymbol{Z}_E \end{bmatrix}^{-1} \begin{bmatrix} -\boldsymbol{V}^r + \boldsymbol{V}^\phi \\ \boldsymbol{V}^r \end{bmatrix}, \tag{9}$$

where the prime ($'$) denotes Hermitian transpose.

The voltages induced across the $C^r_{n_{\boldsymbol{\phi}}}$ capacitances ($\boldsymbol{V}^{sr}$) are

$$\boldsymbol{V}^{\boldsymbol{sr}}_{n_\phi} = \left(\boldsymbol{I}^r_{n_\phi} - \boldsymbol{I}^\phi_{n_\phi - 1}\right) / j\omega C^{\boldsymbol{r}}_{n_{\boldsymbol{\phi}}}. \tag{10}$$

Therefore, the effective-medium μ_z and ε_r obtained from (6a) and (6b) in terms of the voltages and currents are

$$\mu_z = \left(1 - j\frac{\omega\mu_0 t_r \pi (b+a) \boldsymbol{I}^\phi \cdot (\boldsymbol{V}^\phi / \left|\boldsymbol{V}^\phi\right|)}{N_\phi \Delta z \left|\boldsymbol{V}^\phi\right|_1}\right), \tag{11a}$$

$$\varepsilon_r = 1/\left(1 + \left(\boldsymbol{V}^{sr} \cdot \left(\boldsymbol{V}^r / \left|\boldsymbol{V}^r\right|\right) / \left|\boldsymbol{V}^r\right|\right)\right). \tag{11b}$$

For $Z^\phi_{n_\phi} = 1/j\omega C^\phi$ and $Z^r_{n_\phi} \to \infty$ the induced currents $\boldsymbol{I}^\phi$ are

$$\boldsymbol{I}^\phi = \boldsymbol{V}^\phi / \left(j\omega L^{\boldsymbol{\phi}} + 1/j\omega C^\phi\right) \tag{12}$$

and (11a) simplifies to

$$\mu_z = \left(1 - \frac{\mu_0 t_r \pi (b+a)}{\Delta z L^\phi \left(1 - \omega^2_{0m}/\omega^2\right)}\right), \tag{13}$$

where the resonance frequency of ϕ-directed impedances is $\omega_{0m} = 1/\sqrt{L^\phi C^\phi}$. This form is comparable to that of a split-ring resonator, summarized in equation (20) of Ref. [53]. For $Z^\phi_{n_\phi} \to \infty$ and $Z^r_{n_\phi} = j\omega L^r$

$$\boldsymbol{I}^r = \boldsymbol{V}^r / \left(j\omega L^r + 1/j\omega C^{\boldsymbol{r}}\right), \tag{14}$$

and (11b) simplifies to

$$\varepsilon_r = \left(1 - \omega^2_p/\omega^2\right), \tag{15}$$

with plasma frequency $\omega_p = 1/\sqrt{L^r C^r}$, which is approximately equal to the EH_{01} mode cutoff [27], [30]. Equation (15) is the Drude dispersion without damping, which describes the permittivity dispersion of a metallic 3D lattice microstructure comprising a regular array of thin wires [58]. Thus, (13) and (15) show that the ε_r of each mode will follow a Drude dispersion and μ_z will be near unity if $C^\phi \to 0$, so $Z^\phi_{n_\phi} \to \infty$ and $\omega_{0m} \to \infty$, which was assumed in previous works [27], [30].

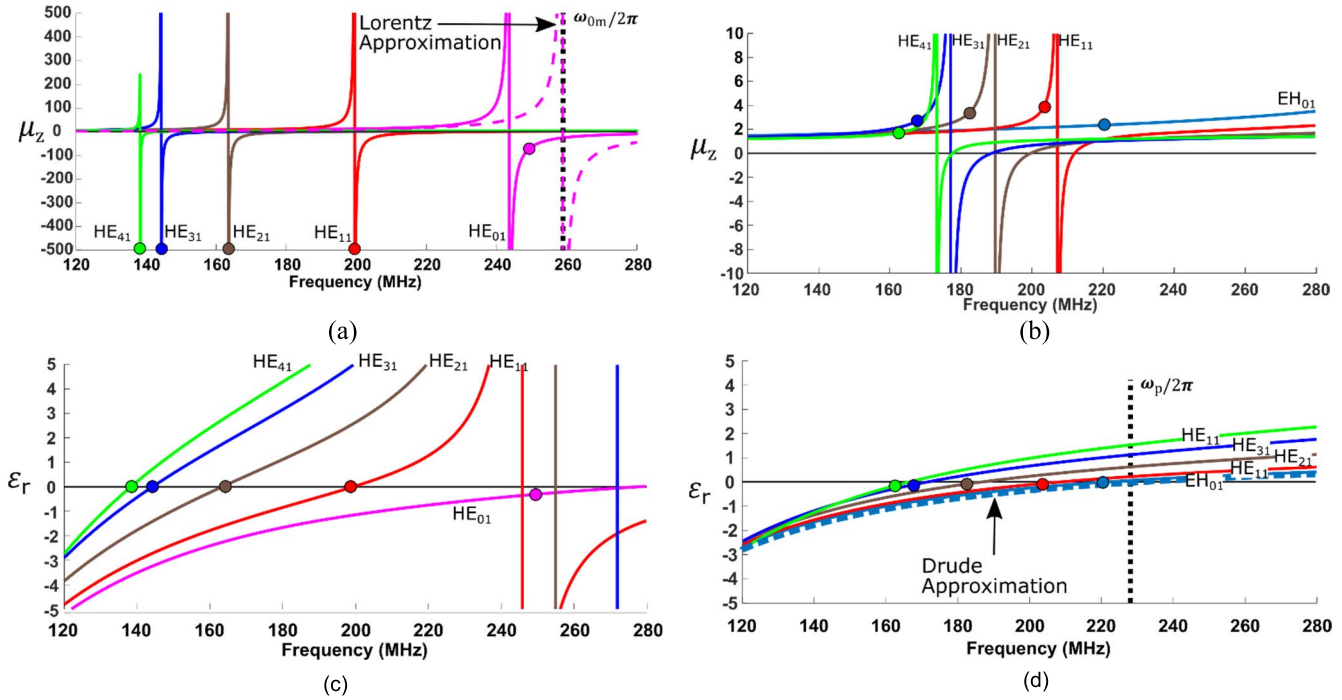

FIGURE 5. Effective μ_z with the (a) MNL or (b) ENNZ case and ε_r for the (c) MNL or (d) ENNZ case for different waveguide HE_{n1} modes . The location of HE_{n1} cutoffs are indicated by round markers on the lines.

III. MM LINER DISPERSION

A. EFFECTIVE PERMEABILITY AND PERMITTIVITY

The intrinsic inductance per segment for both cases was set as $L^{\phi} = 40$ nH. However, to better match the results of full-wave simulation of the dispersion (detailed in Section III.B) the intrinsic radial capacitance was slightly different for the two cases: $C^{r} = 1.77$ pF for the MNL case and $C^{r} = 1.43$ pF for the ENNZ case. The voltage and current distributions of the ENNZ and MNL cases will differ to some extent, so the circuit equivalent values in the EMM are expected to differ slightly.

For the two cases, Fig. 5 shows the effective-medium values calculated from Eqs. (11a) and (11b), and corresponding HE_{n1} cutoff from (1a). For the MNL case, when $n > 0$ the cutoffs occur at frequencies below the μ_z poles (where $\varepsilon_r = 0$). For $n = 0$, the cutoff occurs higher in frequency than the μ_z pole, where both μ_z and ε_r are non-zero and negative (see Fig. 2). For the ENNZ case the cutoffs occur when μ_z is positive and much smaller in magnitude (<4) compared to the MNL case. Furthermore, the cutoffs occur when $\varepsilon_r = 0$ for the EH_{01} case, and when ε_r is negative and near zero for the $n > 0$ cases.

The novelties of this analysis compared to previous work [27], [30] are the description of the MNL case, and the need for different Drude-like permittivity responses to accurately predict the cutoffs for each ENNZ mode. Furthermore, the effective μ_z was assumed to be near unity in the ENNZ case. Finally, because $\overrightarrow{\boldsymbol{D}}^{ir}$ and $\overrightarrow{\boldsymbol{H}}^{iz}$ depend on n (see (5)), so will μ_z and ε_r defined in (11a/b) and the EMM is non-local. In the case presented here, the non-local constitutive parameters converge to local ones in the long-wavelength limit: the constitutive relations for the EH_{01} and HE_{01} modes fit this criterion and are approximated by the Lorentz-type permeability and Drude-type permittivity relations given in Eqs. (13) and (15), respectively. However, these approximations are of limited use in the derivation of the higher order mode cutoffs and propagation curves, such as the HE_{11} mode for operation in this study.

How many segments the cylindrical geometry is divided into is another consideration in deriving constitutive parameters for the liner region (8 segments here). Due to the cylindrical geometry and the N_{seg} periodicity, only integer values of the azimuthal mode orders up to half that of the number of segments are allowed, and therefore the derived constitutive parameters are valid only for those values. The waveguide can only support electromagnetic propagation with those azimuthal variations and the response to impinging fields will be a linear combination of the response of the allowable azimuthal modes.

In summary, the criterion used in this study for the applicability of the EMM model follows that stated in Ref. [41]: "The homogenization has sense if its result (the effective material parameters) can be used for solving boundary problems of electrodynamics where a discrete set of scattering particles is replaced by a sample of a continuous medium." Thus, the constitutive parameters derived here (μ_z and ε_r) have the following limited definition: the replacement of the region composed of the space between MM rings and outer conductor with a homogeneous material, with the constitutive parameters derived, can be used in the analytical

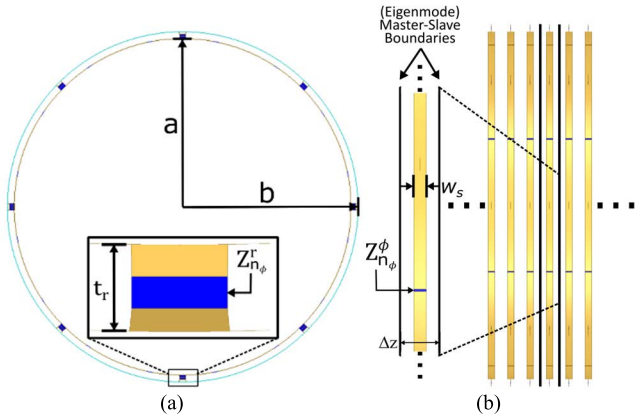

FIGURE 6. MM liner simulation model in a (a) transverse view and (b) side view with labelled lumped impedances. The single ring unit cell is outlined by the inset.

boundary solution of the geometry shown in Fig. 1(a). Thus, the propagation constant and the surface-averaged E-field and H-field can be approximated by the boundary problem solution.

With the EMM developed, the methods of [27] can be used to determine the propagation more accurately; this will be demonstrated in the next section by comparison to full-wave simulation. Its usefulness is highlighted by the resulting close match of the behaviour of the dispersion curves for a large range of frequency when applying the analytical solution with derived bulk constitutive parameters.

B. TUNING AND COMPARISON WITH SIMULATION

The changes in dispersion, cutoff and mode spacing as a function of the equivalent circuit model parameters are demonstrated in the supplementary material.[2] This section covers the determination of the EMM parameters to match dispersion and cutoffs obtained from full-wave analysis of the MM liner structure. The objective is to find a design where the phase shift produces a $\sim \lambda/2$ resonance along a length of MM-lined MRI bore, so that the extent of the magnetic field produced is comparable to the imaging field-of-view of the scanner ($\sim$25 cm). For a typical bore length of 1–2 m only a portion of the bore would include the liner. An 80 cm length of liner is used here, which is near the free-space $\lambda/2 = 0.75$ m for 4.7 T (200 MHz).

The eigenmode simulator in HFSS (Ansys, Canonsburg, PA) was used to find the dispersion curves. A single ring of longitudinal extent Δz is used as a unit cell with master-slave boundaries on the faces of the thin cylindrical volume as labelled in the structure in Fig. 6(b). The eigenmode frequencies were solved for each $\pi/60$ phase step between faces (Fig. 7).

The thin conductive strips making up the rings are backed by the conductive shield of the waveguide or bore, much like microstrip lines, but the fields are altered due to the presence of the adjacent rings. Nevertheless, for the EMM to correctly model the structure in Fig. 6, the values of C^r and L^ϕ are expected to be between those calculated for biplanar lines and those calculated for a microstrip segment of $2\pi a/N_\phi = 7.04$ cm length. Thus, calculated from quasistatic models we would expect 31.0 nH$< L^\phi <$ 97.3 nH (microstrip $<$ biplanar lines) [59] and $0.57pF < C^r < 1.78$ pF (biplanar lines $<$ microstrip) [60]. Considering this appreciable range, the models were tuned by first adjusting L^ϕ so the HE_{01} mode cutoffs matched in the MNL cases, then C^r was adjusted so the EH_{01} mode cutoffs matched in the ENNZ cases.

The C^ϕ capacitor values and L^r inductor were 0.25 pF and 2 nH lower for the full-wave simulation than the values used for the EMM, respectively. The values are higher in the EMM to account for the small additional stray capacitance introduced by the physical gap between conductors where the

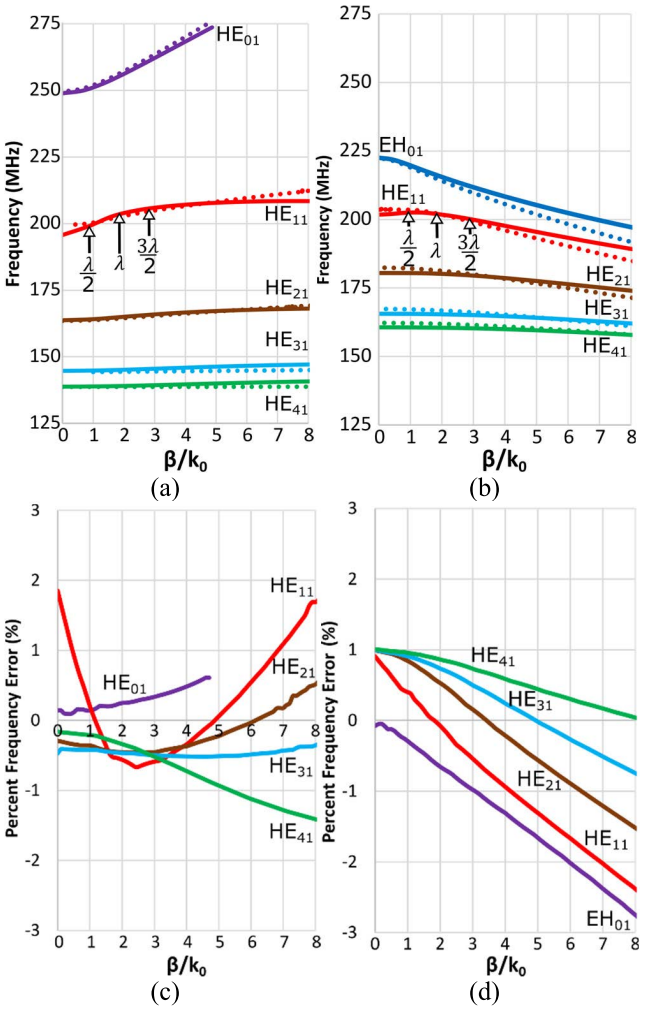

FIGURE 7. Dispersion curves (β/k_0) for the MM lined waveguide modes for (a) MNL and (b) ENNZ cases found using the EMM (dots) or full-wave simulation (solid lines). Arrows indicate different longitudinal resonances ($\lambda/2$, λ, $3\lambda/2$) for the HE_{11} mode with a 80 cm long MM liner. The percent error difference in the EMM vs. simulation model predicted frequency vs. β/k_0 is also shown for the (c) MNL and (d) ENNZ cases.

[2]Supporting document contains results of the dispersion with varying circuit model parameters (Supplementary Material II. Variation of EMM Circuit Parameters).

C^{ϕ} capacitors are, and to account for the small inductance of the radial galvanic connection between the rings and the outer MRI shield/bore. These two parameters affect the spacing of modes.

Therefore, the simulation parameters of the two cases are summarized as follows:

- Fig. 7(a) - MNL, $C^{\phi} = 2.9$ pF, $L^{r} = 50$ nH
- Fig. 7(b) - ENNZ, $C^{\phi} = 0.5$ pF, $L^{r} = 108$ nH

Relating the EMM-predicted dispersion in Fig. 7 to effective medium values in Fig. 5 demonstrates that the MNL is forward propagating (i.e., with parallel phase and group velocities), while the ENNZ is, as observed in previous studies, backwards propagating (with antiparallel phase and group velocities).

The percent difference in the frequency prediction vs. β/k_0 shown in Fig. 7(c/d) demonstrates the close agreement between mode cutoffs predicted from eigenmode simulation and the EMM framework. The MM liner can be designed efficiently to match the desired cutoffs within a 1% difference compared to the eigenmode simulation using accurate calculations of only a few readily obtained geometrically-derived impedances in the ring structures. However, as β/k_0 increases the discrepancy between the eigenmode (considered the ground-truth) and EMM model prediction increases.

The bilayer infinite current sheet representation is a simple and effective model because the fields induced by the transverse currents are confined to the liner region and are directly related to the currents and voltages. However, capacitive coupling between rings introduces longitudinal currents, so fields are not strictly confined to the liner region [27], [30]. This is a cause of some of the (minor) discrepancy in the analytical vs. simulated dispersion in Fig. 7. Additionally, a biaxial permittivity has been assumed in Section II, $\bar{\bar{\varepsilon}}_{\boldsymbol{l}} = \varepsilon_0 \text{diag}(\varepsilon_r, \varepsilon_r, 1)$, which limits the accuracy of the EMM developed here: the radial permittivity ($\varepsilon_r \hat{r}$) is found and assigned equally to the azimuthal permittivity ($\varepsilon_{\phi}\hat{\phi}$). The effect of this assumption is demonstrated in the supplementary material, by comparing the dispersions obtained in three cases: $\bar{\bar{\varepsilon}}_{\boldsymbol{l}} = \varepsilon_0 \text{diag}(\varepsilon_r, \varepsilon_r, 1)$, $\bar{\bar{\varepsilon}}_{\boldsymbol{l}} = \varepsilon_0 \text{diag}(\varepsilon_r, 1, 1)$ and[3] $\bar{\bar{\varepsilon}}_{\boldsymbol{l}} = \varepsilon_0 \text{diag}(1, \varepsilon_r, 1)$. The results suggest that $\varepsilon_{\phi}\hat{\phi}$ has a minimal effect on the dispersion and so the biaxial permittivity approximation is valid for describing the MM liner.

Ideally, a fully descriptive EMM would consider the full anisotropic material property tensors including the impact of longitudinal currents and coupling between rings. In the same way that an impinging field inducing r-directed electric fields and ϕ-directed currents on the MM liner, periodic ring structures are modelled as an effective ε_r and μ_z, z-directed currents and electric fields could be modelled as effective ε_z and μ_{ϕ}. In the case that there is no longitudinal current path or connection between rings through stray capacitance or galvanic contact the ε_z and μ_{ϕ} are unity. In the MM liner presented here the spacing between rings is sufficient that the capacitive coupling is negligible. In addition, at the HE_{n1} cutoffs there is no voltage or phase difference between the rings, and therefore z-directed currents or E-fields will not be induced in any case. Thus, the model can predict the HE_{n1} cutoffs even in the presence of non-unity ε_z and μ_{ϕ}.

As β/k_0 increases, the voltage difference between rings will change in proportion to the propagation factor ($e^{-\gamma z}$), giving rise to induced z-directed currents. In this case including the effective ε_z and μ_{ϕ} would alter the propagation constant (γ) derived via the transcendental equations. Part of the error with increasing β/k_0 shown in Fig. 7 (c-d) is due to this interaction, particularly with the ENNZ case where the C_{ϕ} capacitance is small and therefore closer in magnitude to the z-directed stray capacitance. If the capacitance between rings is increased (e.g., reducing spacing or intentionally adding electrical connections) it would be necessary to include a more complicated EMM model, or to account for coupling between rings and longitudinal currents with a full network model of the MM liner as presented in the Part 2 companion paper [50]. An effective medium model is not included in the Part 2 companion paper, and the dispersion is derived differently. The Part 2 companion paper also validates the assertion that the longitudinal connections do not alter cutoff, and minimally effect the dispersion near cutoff.

The simulated electric and magnetic fields for 1 J of energy stored in each mode are shown in Fig. 8. From these field plots it is observed that only the HE_{11} mode produces the uniform transverse H-field required for MR excitation. There are observable differences in the field profiles of the MNL or ENNZ cases due to the slightly different induced current expected from Eq. (9) because of the different impedance distributions along the ring. As expected, strong transverse electric fields and longitudinal magnetic fields are observed in the liner region, which are accounted for in the EMM by the effective ε_r near zero and large μ_z, respectively.

IV. SIMULATION OF MM-LINED MRI BORE

From either the EMM or full-wave eigenmode simulation the predicted frequency for a desired $\lambda/2$ longitudinal resonance mode along a waveguide is indicated by labelled arrows on the dispersion graphs (Fig. 7). Thus, a full-scale liner consisting of $N_z = 27$ rings was simulated with the dimensions shown in Fig. 9(a), including an MM-lined section of waveguide suitable for providing body MR excitation at 4.7 T (200 MHz). The radius of the waveguide matches that of the 4.7 T MR bore (1.72 m length and 0.28 m radius) available for future testing at the University of Alberta. A $\lambda/2$ resonance is predicted at ~200MHz for the cases presented in Fig. 7. The lined section is placed between two larger-radius vacuum-filled waveguides, with PEC boundaries on outer faces, that are above cutoff for the HE_{11} (TE_{11}) mode to couple the lined waveguide to the simulation ports. The two above-cutoff waveguides are fed by TE_{11} wave ports and thus only HE_{11} propagation is investigated here. Loss in the copper rings and outer

[3]Supporting document contains results of the dispersion with different diagonal permittivity tensors (Supplementary Material III. Evaluation of Biaxial Permittivity Approximation).

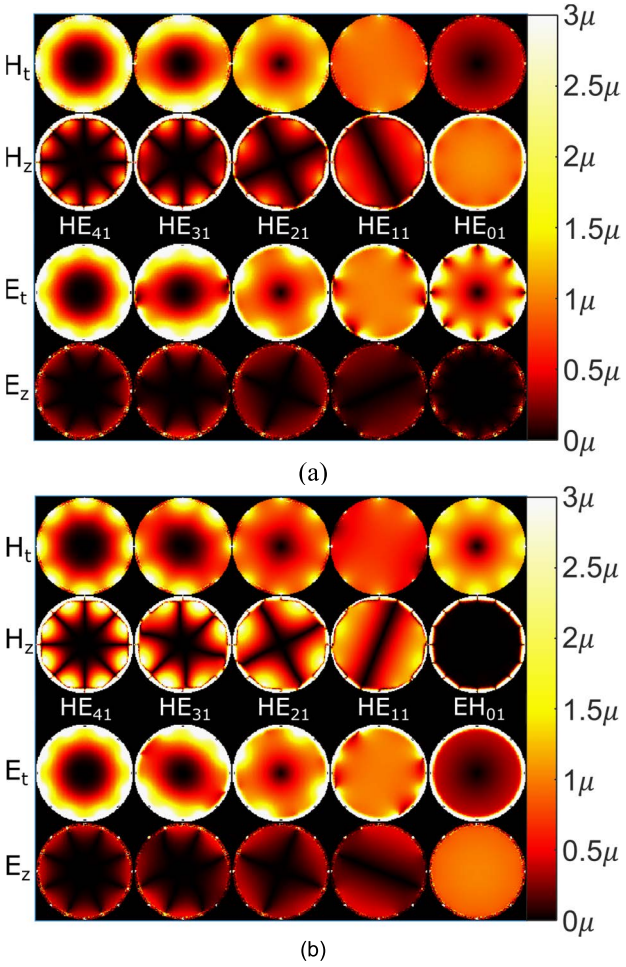

FIGURE 8. Simulated transverse (subscript T) and longitudinal (subscript Z) E and H fields for (a) MNL and (b) ENNZ cases for various propagating modes for $\beta\Delta z = 12°$. The fields are normalized to the mean within the bore excluding the liner ($r < 0.25m$).

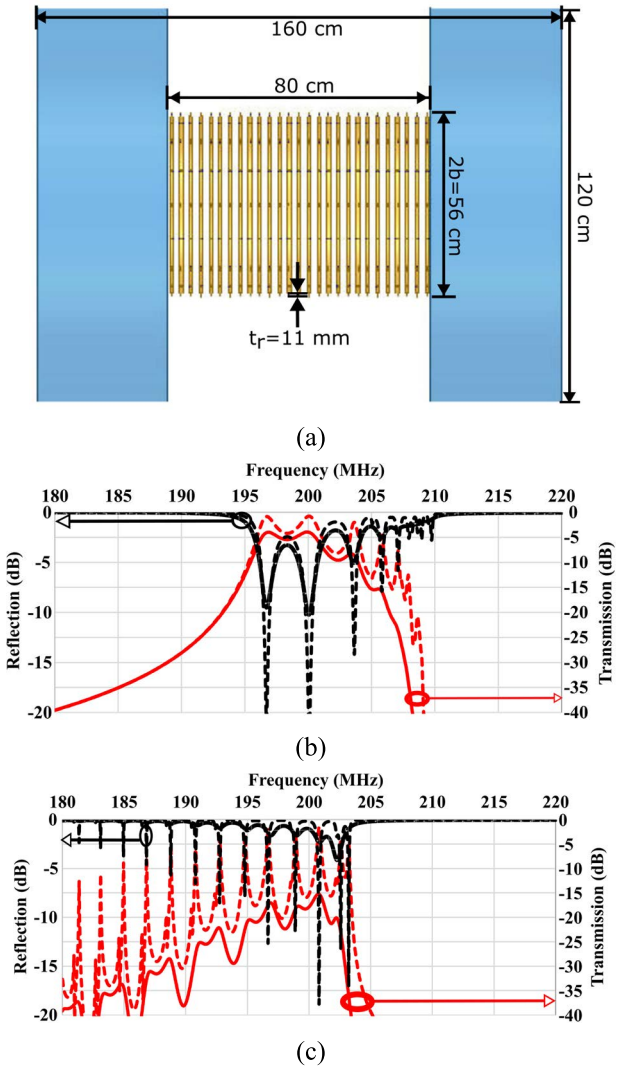

FIGURE 9. (a) Side view of the simulation model employed in the transmission analysis. The transmission (red) and return loss (black) of wave-ports are shown for full-scale liner designed with (b) MNL and (c) ENNZ.

RF shield of the MRI scanner was included (conductivity of 5.8×10^7 S/m). To further model realistic losses, the liner's conductors included a surface roughness of 1 μm and the lumped elements were assigned realistic Q factors at 200 MHz (for the MNL case, $C^\phi = 2.9$ pF with $Q = 1000$ and $L^r = 50$ nH with $Q = 150$; for the ENNZ case, $C^\phi = 0.5$ pF with $Q = 1000$ and $L^r = 108$ nH with $Q = 200$). Finally, a cylindrical phantom (radius = 170 mm, height = 600 mm) roughly matching the electrical properties of the human body/head ($\varepsilon_r = 56$, $\sigma = 0.56$ S/m, [61]) is placed in the center of the bore to investigate its impact on homogeneity for the $\lambda/2$ resonance of the MTM liner for both the MNL and ENNZ cases.

A. SIMULATION WITH UNLOADED BORE

The transmission and reflection parameters of the uniform mode (HE_{11}) for the MNL and ENNZ cases when the bore is empty are shown in Fig. 9(b) and Fig. 9(c), respectively. The bandwidth and magnitude of the transmission peaks are smaller for the ENNZ case compared to the MNL case. When realistic losses are included, the transmission decreases more for the ENNZ case due to the larger, lossy radial inductors. Analyzing the complete full-scale liner presented here using the full-wave simulation method requires extensive simulation time with a dedicated 1TB RAM server. The simulation was used here to benchmark the eigenmode (>15GB RAM and >5 min per point) and EMM methods (<0.5GB RAM and <0.5 min per point) which are computationally orders of magnitude more efficient.

The transverse and longitudinal E and H fields for key resonances/dispersion values (cutoff, $\lambda/2$, λ and $3\lambda/2$) are shown in Fig. 10. For the MNL case distinct longitudinal modes are observed, while for the ENNZ case a mixing of longitudinal modes is observed. For example, there is a strong null in the center of the waveguide for the transverse magnetic field of the cutoff resonance, like that of the λ resonance. This mode mixing results from the ENNZ case flat dispersion curve (Fig. 7(b)).

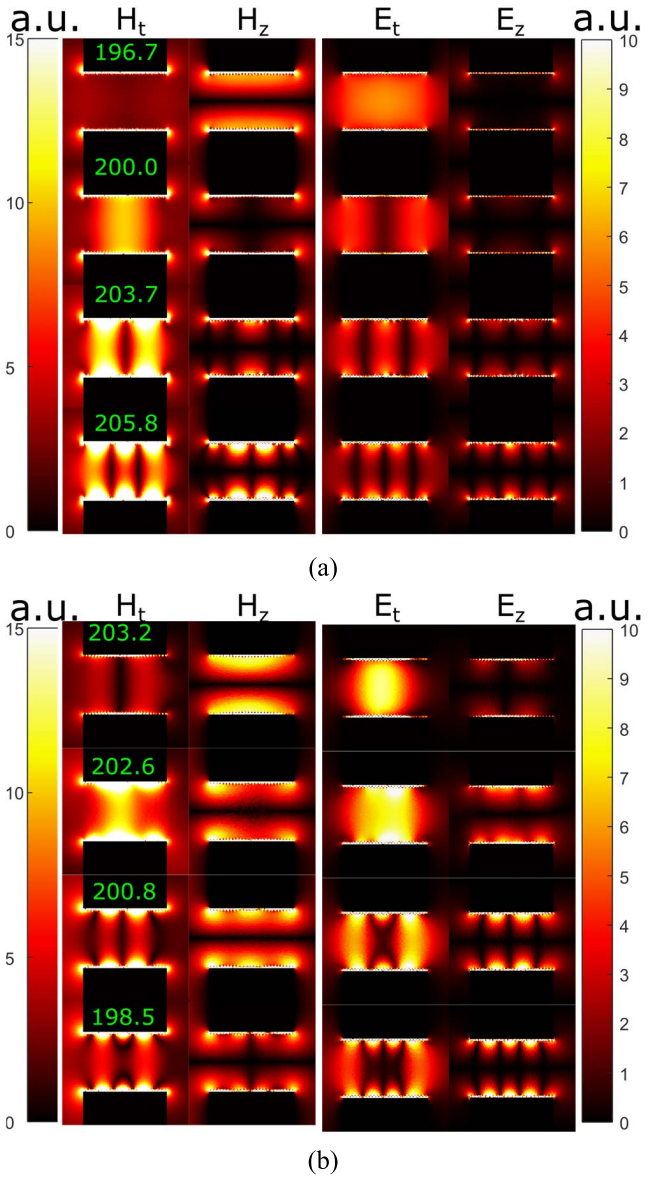

FIGURE 10. Simulated complex magnitudes of the transverse and longitudinal H and E fields in the MM-lined waveguide for the first four transmission peaks in the frequency-reduced (a): MNL forward-wave propagating case and (b): ENNZ backward-wave propagating case.

B. SIMULATION WITH CYLINDRICAL PHANTOM

Transverse and sagittal slices of the simulated transverse and longitudinal E and H fields when a cylindrical phantom is included are shown in Fig. 1(b) The two orthogonal excitations of the TE_{11} mode at one wave port are excited with 90° phase difference to emulate a quadrature excitation relevant for MR excitation. For the MNL case, the fields which are largely homogeneous in the center for the empty bore (Fig. 10(a)) are now inhomogeneous and lower within the phantom. Rings of field nulls are introduced with the characteristic central brightening of the H field observed in other works. Furthermore, the effect of reflections at the transitions between the large waveguide and MM-lined waveguide section are evident, with a strong transverse H-field produced at the transition on the excitation side, and a null present on the opposite side. This highlights a downside of exciting the MM liner travelling wave with an impinging wave, such as with the antennas used in previous works, since longitudinal homogeneities and low transmit efficiency can result from the mismatch of the waves and low coupling between antenna or guiding structure and MM liner. This motivates the use of direct port excitation explored in the companion paper [53], where the simulation of the fields with a realistic human body model is performed and resulting field inhomogeneity is compared between an MM-liner and conventional birdcage coil.

For the ENNZ case the mixing of different longitudinal resonances that was observed with the empty bore is more pronounced when the cylindrical phantom is included (see Fig 1(b)). Overall, the transverse homogeneity is not significantly different from the MNL case, but the presence of multiple nulls and high intensity regions in the longitudinal direction would be detrimental for MRI transmission performance, as well as the lower efficiency due to the higher loss.

V. DISCUSSION

The proposed MM liner is tuned for the $HE_{11}\lambda/2$-resonance (2^{nd} mode in both Fig. 10(a) and (b)), which satisfies the requirements of an effective MR transmit resonator by producing a strong and homogeneous transverse field in the center of an MR-bore sized waveguide. Furthermore, the HE_{11} mode can be driven in quadrature, for more efficient circularly-polarized MR excitation [62]. The newly developed MNL, and existing ENNZ case were compared, and the less desirable properties of the ENNZ case – i.e., more extreme dispersion, smaller transmission bandwidths, mixing of modes, need for large lossy inductors and strong dependence on a parasitic capacitance – favor the MNL case for practical MM liner designs for MRI. However, in both cases the presence of a cylindrical phantom with electrical properties emulating that of the human body causes the fields to become inhomogeneous, due to wavelength effects within the phantom. Thus, determining if the homogeneity is better or comparable to that of a conventional MR transmit resonator (the birdcage coil) is the focus of the companion paper [53]. In addition, the transmission performance metrics of a similarly-designed MNL-case MM liner are compared to those of the conventional birdcage coil at 3 T and 4.7 T with a human body model, demonstrating equivalent transmit efficiency with similar homogeneity and better RF safety (lower SAR) [63], but in both cases inhomogeneous fields are produced within the human body when present.

The MM liner is related to conventional resonators in MRI in some respects. For example, the frequency response of the birdcage coil and TEM resonator also have distinct n-th order azimuthal modes based on the number of rungs/legs of the resonators, which is analogous to the n-th order of the HE_{n1} modes [64], [65]. Additionally, birdcage coils demonstrate increasing or decreasing mode order with

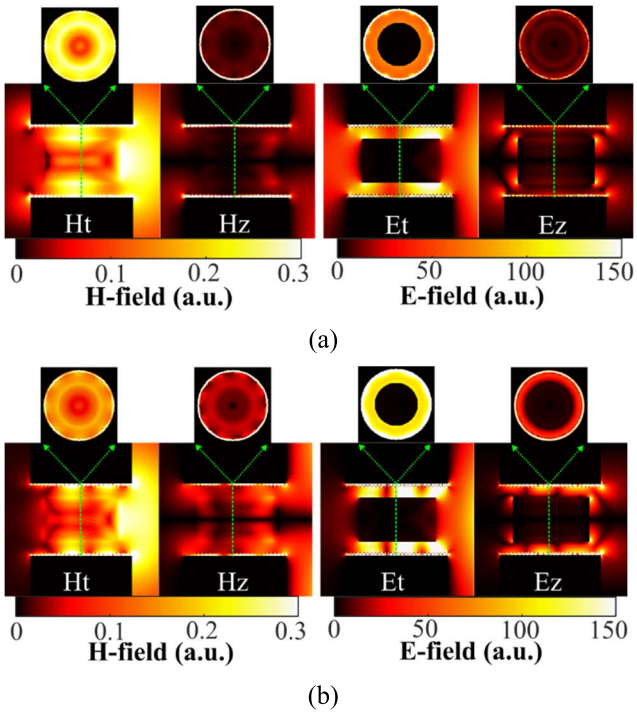

FIGURE 11. Simulated complex magnitudes of the transverse and longitudinal H and E fields in the MM-lined waveguide when filled with a lossy cylindrical phantom (a): MNL forward-wave propagating case at 200MHz and (b): ENNZ backward-wave propagating case at 202.6MHz.

frequency depending on whether the configuration is low-pass or high-pass, respectively. Similarly, the MM liner shows the same behaviour in the MNL case if the radial lumped components are inductive (low-pass) or capacitive (high-pass as demonstrated in Ref [64]). In contrast, due to the longitudinal arrangement of rings the finite length MM liner exhibits longitudinal resonances based on the number of rings. Furthermore, the currents of the MM liner HE_{11} mode are largely azimuthal, while the field-producing currents of the birdcage coil and TEM coil are longitudinal (more akin to the EH_{11} mode).

VI. CONCLUSION

The design of a full-scale MM-lined waveguide has been demonstrated based on two concordant methods of analysis: effective medium analysis with circuit equivalents and full-wave simulation. The EMM developed in Sec. II.C provides a theoretical and conceptual framework for interpreting and understanding the operation of the MM liner designed here for MRI excitation. The method of EMM derivation presented here is applicable to MRI bore liners for various field strengths and bore sizes and may also be applicable to other MM structures.

While the models are valuable design tools, full-wave simulation (Section IV) is still required to determine the MRI performance metrics as well as to verify the final design. Comparison of the MM liner approach to conventional methods of MRI excitation by a birdcage coil and evaluating the impact of realistic body loading is the focus of the Part 2 companion paper [50].

ACKNOWLEDGMENT

The authors would like to thank CMC Microsystems for software access and support by the University of Alberta Faculty of Engineering IT.

REFERENCES

[1] P. L. Robitaille, "Ultra high field magnetic resonance imaging: A historical perspective," in *Ultra High Field Magnetic Resonance Imaging*. Boston, MA, USA: Springer, vol. 26, 2006, pp. 1–17.

[2] A. Laader, K. Beiderwellen, O. Kraff, S. Maderwald, K. Wrede, M. E. Ladd, T. C. Lauenstein, M. Forsting, H. H. Quick, K. Nassenstein, and L. Umutlu, "1.5 versus 3 versus 7 Tesla in abdominal MRI: A comparative study," *PLoS ONE*, vol. 12, no. 11, Nov. 2017, Art. no. e0187528.

[3] *Medical Electrical Equipment: Part 2–33: Particular Requirements for the Basic Safety and Essential Performance of Magnetic Resonance Equipment for Medical Diagnosis*, document IEC 60601-2-33, 2002.

[4] M. A. Erturk, X. Li, P.-F. Van de Moortele, K. Ugurbil, and G. J. Metzger, "Evolution of UHF body imaging in the human torso at 7T: Technology, applications, and future directions," *Topics Magn. Reson. Imag.*, vol. 28, no. 3, pp. 101–124, Jun. 2019.

[5] L. Umutlu, A. K. Bitz, S. Maderwald, S. Orzada, S. Kinner, O. Kraff, I. Brote, S. C. Ladd, T. Schroeder, M. Forsting, G. Antoch, M. E. Ladd, H. H. Quick, and T. C. Lauenstein, "Contrast-enhanced ultra-high-field liver MRI: A feasibility trial," *Eur. J. Radiol.*, vol. 82, no. 5, pp. 760–767, May 2013.

[6] T. Vaughan, L. DelaBarre, C. Snyder, J. Tian, C. Akgun, D. Shrivastava, W. Liu, C. Olson, G. Adriany, J. Strupp, P. Andersen, A. Gopinath, P. van de Moortele, M. Garwood, and K. Ugurbil, "9.4T human MRI: Preliminary results," *Magnetinc Reson. Med.*, vol. 56, no. 6, pp. 1274–1282, 2006.

[7] J. T. Vaughan, G. Adriany, C. J. Snyder, J. Tian, T. Thiel, L. Bolinger, H. Liu, L. DelaBarre, and K. Ugurbil, "Efficient high-frequency body coil for high-field MRI," *Magn. Reson. Med.*, vol. 52, no. 4, pp. 851–859, Oct. 2004.

[8] D. Brunner, N. D. Zanche, J. Frohlich, J. Paska, and K. P. Pruessmann, "Travelling-wave nuclear magnetic resonance," *Nature*, vol. 457, no. 7232, pp. 994–998, Feb. 2009.

[9] X. Yan, X. Zhang, J. C. Gore, and W. A. Grissom, "Improved traveling-wave efficiency in 7T human MRI using passive local loop and dipole arrays," *Magn. Reson. Imag.*, vol. 39, pp. 103–109, Jun. 2017.

[10] B. Zhang, D. K. Sodickson, R. Lattanzi, Q. Duan, B. Stoeckel, and G. C. Wiggins, "Whole body traveling wave magnetic resonance imaging at high field strength: Homogeneity, efficiency, and energy deposition as compared with traditional excitation mechanisms," *Magn. Reson. Med.*, vol. 67, no. 4, pp. 1183–1193, Apr. 2012.

[11] D. O. Brunner, J. Paška, J. Froehlich, and K. P. Pruessmann, "Traveling-wave RF shimming and parallel MRI," *Magn. Reson. Med.*, vol. 66, no. 1, pp. 290–300, Jul. 2011.

[12] S. Alt, M. Müller, R. Umathum, A. Bolz, P. Bachert, W. Semmler, and M. Bock, "Coaxial waveguide MRI," *Magn. Reson. Med.*, vol. 67, no. 4, pp. 1173–1182, Apr. 2012.

[13] A. Andreychenko, J. J. Bluemink, A. J. E. Raaijmakers, J. J. W. Lagendijk, P. R. Luijten, and C. A. T. van den Berg, "Improved RF performance of travelling wave MR with a high permittivity dielectric lining of the bore," *Magn. Reson. Med.*, vol. 70, no. 3, pp. 885–894, Sep. 2013.

[14] G. Wiggins, B. Zhang, R. Lattanzi, and D. Sodickson, "Mid-bore excitation of traveling waves with an annular ladder resonator for 7T body imaging with reduced SAR," *Proc. 18th Annu. Meeting (ISMRM)*, Stockholm, Sweden, 2010, p. 429.

[15] X. Yan, J. C. Gore, and W. A. Grissom, "Traveling-wave meets standing-wave: A simulation study using pair-of-transverse-dipole-ring coils for adjustable longitudinal coverage in ultra-high field MRI," *Concepts Magn. Reson. B, Magn. Reson. Eng.*, vol. 48B, no. 4, Oct. 2018, Art. no. e21402.

[16] T. Herrmann, T. Liebig, J. Mallow, C. Bruns, J. Stadler, J. Mylius, M. Brosch, J. T. Svedja, Z. Chen, A. Rennings, H. Scheich, M. Plaumann, M. J. B. Hauser, J. Bernarding, and D. Erni, "Metamaterial-based transmit and receive system for whole-body magnetic resonance imaging at ultra-high magnetic fields," *PLoS ONE*, vol. 13, no. 1, Jan. 2018, Art. no. e0191719.

[17] D. Erni, T. Liebig, A. Rennings, N. H. L. Koster, and J. Frohlich, "Highly adaptive RF excitation scheme based on conformal resonant CRLH metamaterial ring antennas for 7-Tesla traveling-wave magnetic resonance imaging," in *Proc. Annu. Int. Conf. IEEE Eng. Med. Biol. Soc.*, Aug. 2011, pp. 554–558.

[18] A. K. Iyer, A. Alu, and A. Epstein, "Metamaterials and metasurfaces—Historical context, recent advances, and future directions," *IEEE Trans. Antennas Propag.*, vol. 68, no. 3, pp. 1223–1231, Mar. 2020.

[19] G. V. Eleftheriades, A. K. Iyer, and P. C. Kremer, "Planar negative refractive index media using periodically L-C loaded transmission lines," *IEEE Trans. Microw. Theory Techn.*, vol. 50, no. 12, pp. 2702–2712, Dec. 2002.

[20] A. Shchelokova, R. Schmidt, A. Slobozhanyuk, T. Kallos, A. Webb, and P. A. Belov, "Enhancement of magnetic resonance imaging with metasurfaces: From concept to human trials," in *Proc. 11th Int. Congr. Engineered Mater. Platforms Novel Wave Phenomena (Metamaterials)*, Aug. 2017, pp. 31–33.

[21] R. Schmidt, A. Slobozhanyuk, P. Belov, and A. Webb, "Flexible and compact hybrid metasurfaces for enhanced ultra high field *in vivo* magnetic resonance imaging," *Sci. Rep.*, vol. 7, no. 1, p. 1678, Dec. 2017.

[22] R. Schmidt and A. Webb, "Metamaterial combining electric- and magnetic-dipole-based configurations for unique dual-band signal enhancement in ultrahigh-field magnetic resonance imaging," *ACS Appl. Mater. Interfaces*, vol. 9, no. 40, pp. 34618–34624, 2017.

[23] A. Hurshkainen, A. Nikulin, E. Georget, B. Larrat, D. Berrahou, A. L. Neves, P. Sabouroux, S. Enoch, I. Melchakova, P. Belov, S. Glybovski, and R. Abdeddaim, "A novel metamaterial-inspired RF-coil for preclinical dual-nuclei MRI," *Sci. Rep.*, vol. 8, no. 1, p. 9190, Dec. 2018.

[24] M. J. Freire, L. Jelinek, R. Marques, and M. Lapine, "On the applications of r=−1 metamaterial lenses for magnetic resonance imaging," *J. Magn. Reson.*, vol. 203, no. 1, pp. 81–90, Mar. 2010.

[25] C. Jouvaud, R. Abdeddaim, B. Larrat, and J. de Rosny, "Volume coil based on hybridized resonators for magnetic resonance imaging," *Appl. Phys. Lett.*, vol. 108, no. 2, Jan. 2016, Art. no. 023503.

[26] A. Nikulin, J. de Rosny, K. Haliot, B. Larrat, and A. Ourir, "Opencage radio frequency coil for magnetic resonance imaging," *Appl. Phys. Lett.*, vol. 114, no. 5, Feb. 2019, Art. no. 053503.

[27] J. G. Pollock and A. K. Iyer, "Below-cutoff propagation in metamaterial-lined circular waveguides," *IEEE Trans. Microw. Theory Techn.*, vol. 61, no. 9, pp. 3169–3178, Sep. 2013.

[28] J. D. Jackson, *Classic Electrodynamics*, 3rd ed. Hoboken, NJ, USA: Wiley, 1999.

[29] J. G. Pollock, A. K. Iyer, D. Pratap, and S. A. Ramakrishna, "A class of circular waveguiding structures containing cylindrically anisotropic metamaterials: Applications from radio frequency/microwave to optical frequencies," *J. Appl. Phys.*, vol. 119, no. 8, Feb. 2016, Art. no. 083103.

[30] J. G. Pollock and A. K. Iyer, "Experimental verification of below-cutoff propagation in miniaturized circular waveguides using anisotropic ENNZ metamaterial liners," *IEEE Trans. Microw. Theory Techn.*, vol. 64, no. 4, pp. 1297–1305, Apr. 2016.

[31] J. G. Pollock and A. K. Iyer, "Miniaturized circular-waveguide probe antennas using metamaterial liners," *IEEE Trans. Antennas Propag.*, vol. 63, no. 1, pp. 428–433, Jan. 2015.

[32] N. Hosseini, J. Pollock, A. Iyer, and N. De Zanche, "Metamaterial bore liners as high-field body transmit coils: Advantages over standard birdcage coils," in *Proc. 27th Annu. Meeting (ISMRM)*, 2018, p. 4298.

[33] J. Pollock, N. De Zanche, and A. Iyer, "Traveling-wave MRI at lower B0 field strengths using metamaterial liners," in *Proc. 20th Annu. Meeting (ISMRM)*, 2012, p. 2792.

[34] C. R. Simovski and S. A. Tretyakov, "Local constitutive parameters of metamaterials from an effective-medium perspective," *Phys. Rev. B, Condens. Matter*, vol. 75, no. 19, May 2007, Art. no. 195111.

[35] L. D. Landau, J. S. Bell, M. J. Kearsley, L. P. Pitaevskii, E. M. Lifshitz, and J. B. Sykes, *Electrodynamics of Continuous Media*, 2nd ed. Cambridge, U.K.: Elsevier, 1984.

[36] C. R. Simovski, "Material parameters of metamaterials (a review)," *Opt. Spectrosc.*, vol. 107, no. 5, p. 726, 2009.

[37] D. R. Smith, D. C. Vier, T. Koschny, and C. M. Soukoulis, "Electromagnetic parameter retrieval from inhomogeneous metamaterials," *Phys. Rev. E, Stat. Phys. Plasmas Fluids Relat. Interdiscip. Top.*, vol. 71, Mar. 2005, Art. no. 036617.

[38] K. J. Chau, "Homogenization of waveguide-based metamaterials by energy averaging," *Phys. Rev. B, Condens. Matter*, vol. 85, no. 12, Mar. 2012, Art. no. 125101.

[39] V. V. Gozhenko, A. K. Amert, and K. W. Whites, "Homogenization of periodic metamaterials by field averaging over unit cell boundaries: Use and limitations," *New J. Phys.*, vol. 15, no. 4, Apr. 2013, Art. no. 043030.

[40] A. Ciattoni and C. Rizza, "Nonlocal homogenization theory in metamaterials: Effective electromagnetic spatial dispersion and artificial chirality," *Phys. Rev. B, Condens. Matter*, vol. 91, no. 18, May 2015, Art. no. 184207.

[41] I. Tsukerman, "Classical and non-classical effective medium theories: New perspectives," *Phys. Lett. A*, vol. 381, no. 19, pp. 1635–1640, May 2017.

[42] K. Mnasri, A. Khrabustovskyi, M. Plum, and C. Rockstuhl, "Retrieving effective material parameters of metamaterials characterized by nonlocal constitutive relations," *Phys. Rev. B, Condens. Matter*, vol. 99, no. 3, Jan. 2019, Art. no. 035442.

[43] B. Janaszek and P. Szczepański, "Effect of nonlocality in spatially uniform anisotropic metamaterials," *Opt. Exp.*, vol. 28, no. 10, pp. 15447–15458, 2020.

[44] S. V. Zhukovsky, A. Andryieuski, O. Takayama, E. Shkondin, R. Malureanu, F. Jensen, and A. V. Lavrinenko, "Experimental demonstration of effective medium approximation breakdown in deeply subwavelength all-dielectric multilayers," *Phys. Rev. Lett.*, vol. 115, no. 17, Oct. 2015, Art. no. 177402.

[45] H. Uematsu, L. Dougherty, M. Takahashi, Y. Ohno, M. Nakatsu, M. D. Schnall, and H. Hatabu, "Abdominal imaging at 4T MR system: A preliminary result," *Eur. J. Radiol.*, vol. 47, no. 2, Aug. 2003, doi: 10.1016/s0720-048x(02)00195-x.

[46] L. Dougherty, T. J. Connick, and G. Mizsei, "Cardiac imaging at 4 Tesla," *Magn. Reson. Med.*, vol. 45, no. 1, pp. 176–178, Jan. 2001.

[47] S. M. Hussain, P. A. Wielopolski, and D. R. Martin, "Abdominal magnetic resonance imaging at 3.0 T: Problem or a promise for the future?" *Topics Magn. Reson. Imag.*, vol. 16, no. 4, pp. 325–335, Jul. 2005, doi: 10.1097/01.rmr.0000224689.06501.16.

[48] H. Uematsu, L. Dougherty, M. Takahashi, Y. Ohno, M. Nakatsu, H. K. Song, V. A. Ferrari, W. B. Gefter, M. D. Schnall, and H. Hatabu, "Pulmonary MR angiography with contrast agent at 4 Tesla: A preliminary result," *Magn. Reson. Med.*, vol. 46, no. 5, pp. 1028–1030, Nov. 2001, doi: 10.1002/mrm.1292.

[49] A. Laader, K. Beiderwellen, O. Kraff, S. Maderwald, K. Wrede, M. E. Ladd, T. C. Lauenstein, M. Forsting, H. H. Quick, K. Nassenstein, and L. Umutlu, "1.5 versus 3 versus 7 Tesla in abdominal MRI: A comparative study," *PLoS ONE*, vol. 12, no. 11, Nov. 2017, Art. no. e0187528, doi: 10.1371/journal.pone.0187528.

[50] A. Maunder, A. K. Iyer, and N. De Zanche, "Metamaterial liner for MRI excitation: Design and performance at 4.7T," *IEEE Trans. Med. Imag.*, vol. 10, 2022, doi: 10.1109/ACCESS.2022.3167764.

[51] S. W. Ellingson, *Electromagnetics*, vol. 1. Blacksburg, VA, USA: VT Publishing, 2018.

[52] S. Hrabar, Z. Eres, and J. Bartolic, "Capacitively loaded loop as basic element of negative permeability meta-material," in *Proc. 32nd Eur. Microw. Conf.*, Oct. 2002, pp. 1–4.

[53] J. B. Pendry, A. J. Holden, D. J. Robbins, and W. J. Stewart, "Magnetism from conductors and enhanced nonlinear phenomena," *IEEE Trans. Microw. Theory Techn.*, vol. 47, no. 11, pp. 2075–2084, Nov. 1999.

[54] W. Lamb, D. M. Wood, and N. W. Ashcroft, "Long-wavelength electromagnetic propagation in heterogeneous media," *Phys. Rev. B, Condens. Matter*, vol. 21, no. 6, pp. 2248–2266, Mar. 1980.

[55] D. R. Smith, D. C. Vier, N. Kroll, and S. Schultz, "Direct calculation of permeability and permittivity for a left-handed metamaterial," *Appl. Phys. Lett.*, vol. 77, no. 14, pp. 2246–2248, Oct. 2000.

[56] D. R. Smith and J. B. Pendry, "Homogenization of metamaterials by field averaging (invited paper)," *J. Opt. Soc. Amer. B, Opt. Phys.*, vol. 23, no. 3, pp. 391–403, 2006.

[57] J.-M. Lerat, N. Malléjac, and O. Acher, "Determination of the effective parameters of a metamaterial by field summation method," *J. Appl. Phys.*, vol. 100, no. 8, Oct. 2006, Art. no. 084908.

[58] J. B. Pendry, A. J. Holden, W. J. Stewart, and I. Youngs, "Extremely low frequency plasmons in metallic mesostructures," *Phys. Rev. Lett.*, vol. 76, no. 25, pp. 4773–4776, Jun. 1996.

[59] C. R. Paul, *Inductance: Loop and Partial*, 2nd ed. Hoboken, NJ, USA: Wiley, 2010.

[60] C. R. Paul, *Analysis of Multiconductor Transmission Lines*, 2nd ed. Hoboken, NJ, USA: Wiley, 2007.

[61] S. B. Bulumulla, S. K. Lee, and D. T. B. Yeo, "Conductivity and permittivity imaging at 3.0T," *Concepts Magn. Reson. B, Magn. Reson. Eng.*, vol. 41B, no. 1, pp. 13–21, Feb. 2012.
[62] D. I. Hoult and P. C. Lauterbur, "The sensitivity of the zeugmatographic experiment involving human samples," *J. Magn. Reson.*, vol. 34, no. 2, pp. 425–433, 1979.
[63] A. Maunder, N. D. Zanche, and A. K. Iyer, "Simulation comparison of birdcage coil and metamaterial liner for MRI at 3T and 4.7T," in *Proc. 50th Eur. Microw. Conf. (EuMC)*, Jan. 2021, pp. 1067–1070.
[64] B. A. Baertlein, O. Ozbay, T. Ibrahim, R. Lee, Y. Yu, A. Kangarlu, and P. M. Robitaille, "Theoretical model for an MRI radio frequency resonator," *IEEE Trans. Biomed. Eng.*, vol. 47, no. 4, pp. 535–546, Apr. 2000.
[65] M. C. Leifer, "Resonant modes of the birdcage coil," *J. Magn. Reson.*, vol. 124, no. 1, pp. 51–60, 1997.

ADAM MITCHELL MAUNDER (Member, IEEE) received the B.Sc. degree in engineering physics and the M.Sc. degree in biomedical engineering from the University of Alberta, Edmonton, AB, Canada, in 2012 and 2013, respectively, and the Ph.D. degree in engineering from The University of Sheffield, Sheffield, U.K., in 2019. He is currently working as a Postdoctoral Fellow with the Oncology Department, University of Alberta.

CHRISTOPHER BARKER (Student Member, IEEE) received the B.Sc. degree in electrical and electronics engineering from the University of Alberta, in 2019, where he is currently pursuing the Ph.D. degree with the Electrical and Computer Engineering Department, with a focus on metasurfaces for cylindrical waveguides.

NICOLA DE ZANCHE (Senior Member, IEEE) received the Laurea degree in electronics engineering from the University of Padova, Padova, Italy, in 1996, and the Ph.D. degree in medical sciences–biomedical engineering from the University of Alberta, Edmonton, Canada, in 2002. From 2002 to 2008, he was a Postdoctoral Fellow and subsequently a Senior Scientist with the Institute for Biomedical Engineering, Swiss Federal Institute of Technology, Zurich, Switzerland, and the University of Zurich, Zurich. He is currently an Associate Professor with the Division of Medical Physics, Department of Oncology, University of Alberta, and a Medical Physicist with Alberta Health Services. He is also a Professional Engineer with the Association of Professional Engineers and a Geoscientists of Alberta. He is certified by the Canadian College of Physicists in Medicine. He lectures on MRI instrumentation and other medical imaging methods. His research interest includes all aspects of RF technology for MRI.

ASHWIN K. IYER (Senior Member, IEEE) received the B.A.Sc. (Hons.), M.A.Sc., and Ph.D. degrees in electrical engineering from the University of Toronto, Toronto, ON, Canada, in 2001, 2003, and 2009, respectively, where he was involved in the discovery and development of the negative-refractive-index transmission-line approach to metamaterial design and the realization of metamaterial lenses for free-space microwave subdiffraction imaging. He is currently a Professor with the Department of Electrical and Computer Engineering, University of Alberta, Edmonton, AB, Canada, where he leads a team of graduate students investigating novel RF/microwave circuits and techniques, fundamental electromagnetic theory, antennas, sensors, and engineered metamaterials, with an emphasis on their applications to microwave and optical devices, defense technologies, and biomedicine. He has coauthored a number of highly-cited papers and four book chapters on the subject of metamaterials. He is a member of the IEEE AP-S Administrative Committee and Education Committee. He is a Registered Member of the Association of Professional Engineers and Geoscientists of Alberta. He was a recipient of the IEEE AP-S R. W. P. King Award, in 2008; the IEEE AP-S Donald G. Dudley Jr. Undergraduate Teaching Award, in 2015; the University of Alberta Provost's Award for Early Achievement of Excellence in Undergraduate Teaching, in 2014; and the University of Alberta Rutherford Award for Excellence in Undergraduate Teaching, in 2018. His students are the recipients of several major national and international awards for their research. He served as the Technical Program Committee Co-Chair for the 2020, 2016, and 2015 AP-S/URSI International Symposia. He serves as the Chair for the IEEE Northern Canada Section's Award-Winning Joint Chapter of the AP-S and MTT-S. From 2012 to 2018, he was an Associate Editor of the IEEE TRANSACTIONS ON ANTENNAS AND PROPAGATION and currently serves as a Track Editor. He was also a Guest Editor of the IEEE TRANSACTIONS ON ANTENNAS AND PROPAGATION for the Special Issue on Recent Advances in Metamaterials and Metasurfaces.